Towards the high-throughput synthesis of bulk materials: thermoelectric PbTe-PbSe-SnTe-SnSe alloys

Journal:	*Molecular Systems Design & Engineering*
Manuscript ID	ME-ART-10-2018-000073.R1
Article Type:	Paper
Date Submitted by the Author:	24-Jan-2019
Complete List of Authors:	Ortiz, Brenden; Colorado School of Mines, Physics Adamczyk, Jesse; Colorado School of Mines, Physics Gordiz, Kiarash; Colorado School of Mines, Physics Braden, Tara; Colorado School of Mines, Physics Toberer, Eric; Colorado School of Mines, Physics

Design, System, Application:

The development of functional materials is becoming an increasingly complex problem. Whether in thermoelectrics, photovoltaics, batteries, or superconductivity, the number of possible tuning parameters (alloying, doping, microstructure) has created an incredibly high-dimensional search space. In response, many groups have begun integrating high-throughput first-principles computation to down select materials and provide guidance for experiment. However, experimental realization of new materials remains an artisanal process driven by serial, intuition driven processes. The integration of high-throughput synthesis, particularly for bulk electronic materials, would represent a significant paradigm shift within materials science. Within this work, we demonstrate the value of high-throughput experimental methods by synthesizing and characterizing 121 samples within the PbTe-PbSe-SnTe-SnSe series of alloys. Our work recreates over 50 years of historical alloying data while simultaneously discovering several new trends. This work motivates and sets the foundation for future efforts to produce a fully high-throughput material optimization facility, combining computation, experiment, and data-driven methods to accelerate the development of next-generation materials.

Journal Name

ARTICLE TYPE

Cite this: DOI: 10.1039/xxxxxxxxxx

Towards the high-throughput synthesis of bulk materials: thermoelectric PbTe-PbSe-SnTe-SnSe alloys

Brenden R. Ortiz,*[a] Jesse M. Adamczyk,[a] Kiarash Gordiz,[a] Tara Braden,[a] and Eric S. Toberer*[a]

Received Date
Accepted Date

DOI: 10.1039/xxxxxxxxxx

www.rsc.org/journalname

The experimental realization of new functional materials is a complex optimization problem that would vastly benefit from the application of high-throughput methodologies. In this work, we adapt bulk ceramic processing for high-throughput integration, with a focus on producing high-quality thermoelectric materials. We also monitor the time and effort cost per sample, providing insight for where additional engineering can further increase throughput. Through parallelization and automation, we achieve a 5-10× increase in synthetic speed, allowing the generation of a 121 sample alloy map within the PbTe-PbSe-SnTe-SnSe system. Despite heavy investment from the thermoelectric community, prior literature exclusively focuses on intuitive pseudobinary combinations within the PbTe-PbSe-SnTe-SnSe alloys. Our intuition-agnostic mapping, however, has enabled us to identify compositions with anomalous, non-monotonic changes in the thermoelectric transport. The newly discovered trends (e.g. high mobility alloys, extended band-inversion region) do not lie on the intuitive pseudobinary combinations – exemplifying the value of unbiased high-throughput methods. Additionally, as our methods were chosen explicitly to preserve sample quality, our solubility limits and room-temperature thermoelectric transport are also in excellent agreement with available literature. Ultimately, this work demonstrates that high-throughput methods are a potent tool for the accelerated optimization and realization of new functional materials.

1 Introduction

Widespread application of high-throughput (HTP) materials science necessitates simultaneous advances in theoretical, computational, and experimental prowess. Particularly in recent years, the Materials Genome Initiative has succeeded in spurring ambitious computational projects aimed to expedite the discovery of new functional materials. From photovoltaics,[1–7] catalysis,[8–15] batteries,[16–22] and thermoelectrics,[23–29] advances in computational power and the application of machine learning are well-poised to launch materials science into a new era. However, experimental synthesis and characterization remains largely driven by serial ("artisanal") techniques that trade speed for accuracy and precision. HTP synthesis is a quickly growing trend within the thin-film community (e.g. photovoltaics), but they are rarely generalized to bulk studies due to restrictions in form-factor, metastability, and elemental composition.[30–42] Physical metallurgy has also experienced a growth in HTP methods, although the processing often relies on melting (e.g. arc-melting, additive manufacturing) and is explicitly focused on mechanical properties.[43–48]. Combinatorial methods examining electronic or thermal transport within bulk ceramic materials are rare, with existing studies focusing on relatively smaller sample sets (<20).[49,50]

For experimental methods to maintain pace with computational and theoretical efforts will require a revolution in the way we synthesize and characterize materials. However, increases in speed cannot be associated with a significant degradation of material quality. Material synthesis must also match both the thermodynamic and form-factor restrictions of the application. Take, for example, the field of thermoelectrics. Computational efforts have spawned multiple searches which have identified potentially revolutionary materials.[23–29,51,52] However, successful thermoelectric materials are *heavily* optimized through a combination of alloying, doping, and nanostructuring.[53–60] As in many fields, the optimization of a thermoelectric material is not only a high-dimensional problem, but also involves nuanced physics. Thus, it is not enough to accelerate the identification new of materials – we must also catalyze their optimization.

Consider PbTe, whose incumbent success as a thermoelectric material is derived from >50 years of research and the confluence of many unusual phenomena.[61] Figure 1 shows a review of the PbTe-PbSe-SnTe-SnSe alloying literature which also contains thermoelectric transport measurements. Only studies that report bulk properties (no thin films or nanostructures) were in-

[a] *Colorado School of Mines, Golden, CO, United States.*

† Electronic Supplementary Information (ESI) available: [details of any supplementary information available should be included here]. See DOI: 10.1039/b000000x/

cluded. Blue dots represent reported compositions, deeper shades of blue indicate repeated compositions through multiple studies. Faint grey dots indicate the compositions studied in this work. Despite heavy academic and industrial investment in PbTe, all reported bulk properties are constrained to the chemically intuitive pseudobinaries.[62–90] However, many of the effects used to produce high efficiency PbTe were not expected from chemical intuition alone and were derived ex-post-facto. For example, alloying PbTe with Se causes a convergence of the electronic band diagram at high-temperature that significantly increases the thermoelectric performance.[64] Doping PbTe with Tl induces localized defect states near the valence band edge (resonant doping) that dramatically increases the Seebeck coefficient.[77,91,92] The serial identification of these effects and the collective optimization of PbTe has involved countless research groups and innumerable human time. Further, we are not guaranteed that all interesting phenomena occur on the pseudobinary alloy combinations. An rapid, unbiased approach to screening alloy compositions would be a great boon to materials optimization efforts.

This work serves as a pilot project – to assess the value of HTP experimental methods within thermoelectrics using the PbTe-PbSe-SnTe-SnSe alloying system. Increases in speed from the automation of powder weighing and the parallelization of hot pressing and ball milling, allows creation of a 121 sample map, the largest singular data set to date in PbTe-based alloys. Our experimentally observed solubility limits and room-temperature thermoelectric transport are in excellent agreement with available literature. Unlike prior literature, our alloying space spans the entire PbTe-PbSe-SnTe-SnSe quaternary space, granting us the ability to resolve new trends. In fact, many of the interesting compositions do not lie upon the chemically intuitive pseudobinary lines, and were not investigated in the previous literature. In addition to the fundamental materials research, we also provide a breakdown of the most time consuming processes during our synthesis and characterization of the 121 sample map. We find that true HTP efforts must simultaneously achieve automation and parallelization, particularly if high-temperature measurements are desired. Ultimately our work further cements the value of HTP experimental efforts, particularly in complex systems with high-dimensional optimization problems.

2 Methods

Batches of precursor PbTe, PbSe, SnTe, and SnSe powders were generated by ball milling stoichiometric mixes of elemental reagents in tungsten carbide ball mill vials under nitrogen. Source materials for all precursor synthesis were Pb granules (Alfa, 99.99%), Sn granules (Alfa, 99.99+%), Te ingot (Alfa 99.999+%), and Se shot (Alfa 99.999+%). To remove oxide coatings from Sn and Pb, the granules were cleaned by submerging in a solution of NaOH (∼1 M), followed by rinsing in anhydrous reagent grade ethanol. The metals were then dried under vacuum and stored in a nitrogen dry box with <1 ppm oxygen and <5 ppm moisture. The ball milled powders were loaded into cleaned fused silica ampules and annealed under vacuum at 75% of the melting point for 12 h. Powders were subsequently ground and passed through a <106 μm mesh sieve. Approximately 250 g

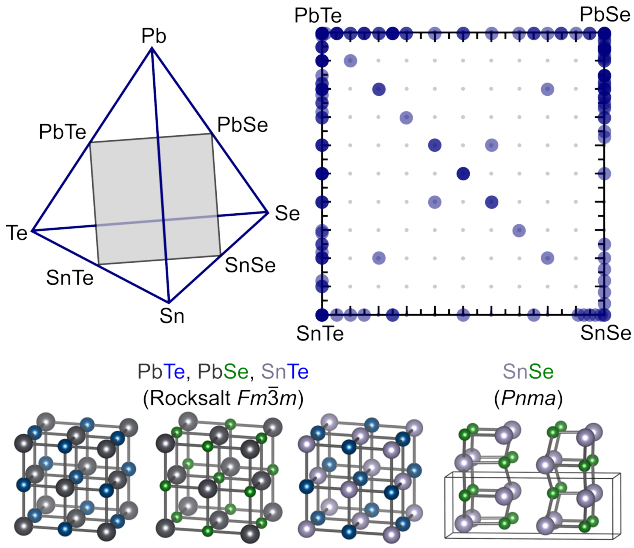

Fig. 1 The Pb-Sn-Te-Se phase diagram (left) contains the four 1:1 binary compounds PbTe, PbSe, SnTe, and SnSe. Alloys between the four binaries are constrained to a square plane, where the corners correspond to the pure binary compounds (right). PbTe, PbSe, and SnTe share the rocksalt $Fm\bar{3}m$ prototype, but SnSe crystallizes in the distorted-rocksalt *Pnma* structure (bottom). Despite including the most heavily studied materials in thermoelectrics, a review of the literature indicates that experimental studies (blue circles) are constrained to pseudobinary combinations. The present study considers alloys on an evenly spaced grid (10% increments), denoted by gray dots.

of each precursor powder were generated. However, as individual batches were limited to ∼25-40 g, we did not begin synthesis of the 121 sample grid until all precursor batches were generated, verified by X-ray diffraction, and homogeneously blended together. This step enables us to have confidence that samples are generated from effectively identical precursors, eliminating batch-to-batch errors.

Precursor powders were loaded into our custom-built automatic weighing system, which can automatically dispense aliquots of each precursor powder with 0.0005 g accuracy. Dispensing was performed in air. The process is comparable in speed to manual weighing, but it requires no human presence. The system can mix up to three precursors at a time, which enables complete coverage of the Pb-Sn-Te-Se grid *via* controlled mixing of either PbTe-SnTe-PbSe or SnTe-PbSe-SnSe. The powders are directly dispensed into 5 mL hardened steel ball mill vials (SPEX 3127) with a 1/4 inch steel ball. Samples were bundled into sets of 8 vials using a multi-sample adaptor (SPEX 8011) and milled for 60 min in a SPEX 8000D high-energy ball mill.

In addition to enabling automatic weighing, the use of precursor powders (as opposed to elemental metals) allows ball milling to act as a *blending* process instead of a *reactive* process. Our milling is not intended to cause mechanical alloying, as is commonly observed in the literature. Indeed, as we monitored the X-ray diffraction of our as-milled powders, we observed only mild alloying as a result of mechanically-induced processes. However, by omitting reactive milling, our process allows us to utilize smaller vials that are easier to parallelize, achieving an 8-16× improvement in milling throughput.

The as-milled precursor mixtures are then loaded into high-density graphite dies. Multiple samples are pressed simultaneously by alternating layers of high-density graphite spacers, graphite foil, and PbSnTeSe powder within the die. The final arrangement repeats as spacer-foil-powder-foil-spacer. The layering of graphite prevents cross-contamination and provides rigidity to the stack during pressing. This allows for a 4-6× factor of improvement in pressing throughput. Note that all graphite (die, spacers, foil) were baked under vacuum to 400°C to remove water and organics before hot pressing. The stacked die is loaded into a uniaxial induction hot press under vacuum. An initial empirical calibration was performed to find the quickest temperature-time profile that enables full densification over all compositions, minimal creep, minimal sublimation, and still achieves thermally-driven alloying. We find that a ramp to 550°C over 15 min followed by a densification step (3 h soak at 550°C and 15 MPa), and a relatively quick cool (2 h to 50°C) are suitable conditions for the entirety of the grid.

After hot pressing, samples are removed from the graphite die and polished. X-ray diffraction (XRD) was performed on each pellet using a Bruker D2 Phaser (Cu K-α radiation) in a θ-2θ configuration from 10-90° of 2θ. Analysis was performed using the TOPAS V6 software package.[93] The data was refined using a mixture of Pawley and Rietveld analysis to extract the lattice parameters, cell volumes, and to identify phase segregation. When needed, scanning electron microscopy was also performed using a JEOL JSM-7000F Field Emission SEM.

Hall effect and resistivity measurements were performed using the Van der Pauw geometry on a home-built apparatus.[94] Measurements were conducted at room-temperature in air with pressure-assisted, nichrome wire contacts. For resistive samples, indium contacts were used to ensure ohmic contacts. Seebeck coefficient measurements were conducted using the quasi-steady slope method at room-temperature in air.[94,95] Thermal diffusivity was measured using a Netzsch Hyperflash (LFA 467) system with a 16× sample adapter at room-temperature. The resulting diffusivity data was fit using a Cowen plus Pulse Correction (CPC) numerical model. The samples were coated with graphite spray prior to measurement to reduce errors in sample emissivity. The thermal conductivity is calculated using the Dulong-Petit approximation for the sample heat capacity. Sample densities were measured using the Archimedes method. Samples are consistently >96% of the theoretical density estimated by XRD.

Whenever a particular sample was prone to skepticism, we performed additional validation using classical synthesis methods. For example, the sample composition $Pb_{0.2}Sn_{0.8}Te_{0.3}Se_{0.7}$ showed unusual phase segregation which could have been ascribed to kinetic limitations. To check for consistency, elemental reagents (Pb, Sn, Te, Se) were ball milled for 90 min in a tungsten carbide ball mill vial, sealed in a fused silica ampule, and annealed for >1 week at 75% of the melting point. The annealed powder was subsequently consolidated via uniaxial hot pressing at 550°C and 15 MPa for 3 h.

To provide a measure of efficiency and process-dependent time consumption, we collected metadata for each process involved during the 121 sample map creation. Time consumption is binned depending on process and whether the time was "machine time" or "human time." We define "machine time" as any process where an instrument is performing an action, but where a human is not required to monitor the process. "Human time" explicitly involves physical or mental engagement of a human. Note that any time taken during data analysis and visualization was not included in our analysis. We also omit the capital (time) cost of building or purchasing any instruments.

3 Results and Discussion

With 121 samples, this investigation into the PbTe-PbSe-SnTe-SnSe alloying system is the largest compilation of bulk thermoelectric samples produced for a single study. Our goals are multifaceted – we aim to provide proof of concept that HTP bulk synthesis can add value to experimental studies and identify where additional engineering can ameliorate potential bottlenecks. Further, this provides an opportunity to investigate the fundamental material science within some of the most industrially relevant thermoelectric compounds. Our study begins with an in-depth assessment of the crystallography, solubility limits, and phase equilibria in the PbTe-PbSe-SnTe-SnSe alloys.

3.1 Structure and Alloying

The development of methods amenable to HTP synthesis cannot come at a significant cost to material quality. Particularly in high-dimensional systems, obtaining homogeneous samples can be a challenging endeavour. Our first investigation into our 121 sample matrix focuses on changes in crystallography (e.g. cell volume) as a function of composition. Successful alloying and identification of phase boundaries within the PbTe-PbSe-SnTe-SnSe plane will not only enable us to assess the viability of our synthetic techniques, but also provide key information through which we interpret electronic and thermal transport data in later sections.

Figure 2 shows our experimentally generated heat maps of the cell volume throughout the entire PbTe-PbSe-SnTe-SnSe quaternary plane. The figure is divided into two plots. Figure 2a shows changes in the rocksalt crystal structure throughout the single-phase and two-phase regions. First and foremost, we note smoothly varying color contours in the heat map, demonstrating excellent alloying. Along the pseudobinary lines (e.g. PbTe-PbSe), we see linear changes in the cell volume with composition, consistent with Vegard's Law. Select traces along the pseudobinary edges of the heat map are shown in the ESI, Figure S1. As one of the single largest agglomerates of data within the PbTe-PbSe-SnTe-SnSe phase space, each heat map is rich with nuanced detail. The raw data is available in the ESI, Figure S2 and S3. In this manuscript we will focus primarily on the strongest features and their connection to the currently available literature.

Consistent with prior literature, we find that all rocksalt phases possess full solid-solubility in one another.[68,74,78,84,86,96,98,99,106–115] However, any pairwise combination of a rocksalt phase with SnSe exhibits significantly reduced solubility. Along the pseudobinary edges (e.g. PbSe-SnSe), a Vegard's Law analysis of the cell volume data allows us to extract the compositions at which solid

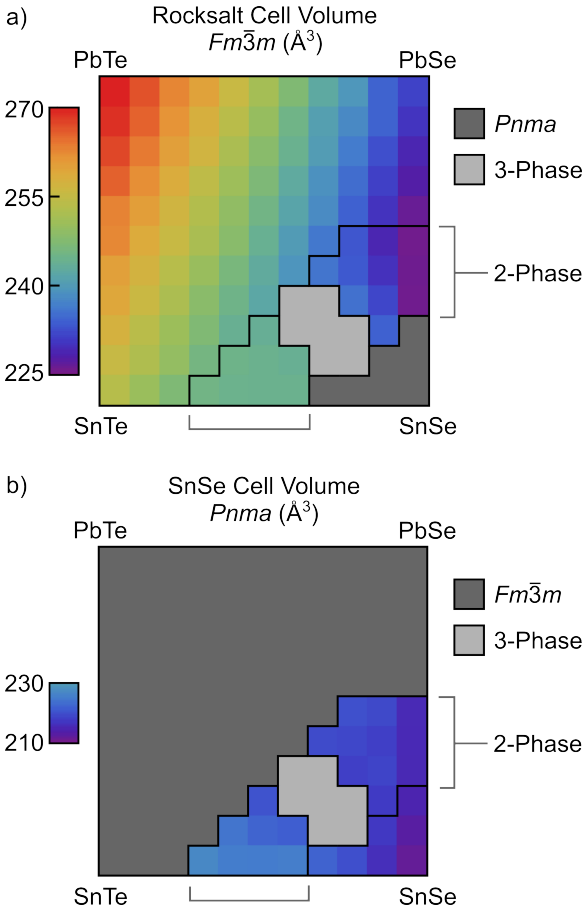

Fig. 2 Cell volume heat maps for the (a) rocksalt alloy and (b) SnSe alloy are shown with sample compositions evenly spaced in 10 mol% increments. The cell volume for both the rocksalt and SnSe phases are shown in their respective regions (colored fill) for all samples where a refinable quantity exists. Black outlines roughly denote phase boundaries; we observe two well-defined two-phase regions (grey brackets) and one three-phase region (light grey fill). All experimentally determined solubility limits are in excellent agreement with literature.[96–105]

solubility terminates. Along the PbSe-SnSe pseudobinary, we find that PbSe integrates a significant amount of Sn (44 % or $Pb_{0.56}Sn_{0.44}Se$) and SnSe integrates a moderate amount of Pb (25 % or $Pb_{0.25}Sn_{0.75}Se$). These results agree well with literature, which quote a solubility range of 37-47 % SnSe in PbSe and 21-25 % PbSe in SnSe, respectively.[98–103] Along the SnTe-SnSe pseudobinary, we find that SnTe integrates a significant amount of Se (28 % or $SnTe_{0.72}Se_{0.28}$) and SnSe integrates a moderate amount of Te (34 % or $SnTe_{0.34}Se_{0.66}$). These results agree well with literature, which quote a solubility of 22-28 % SnSe in SnTe and 25-30 % SnTe in SnSe, respectively.[98,104,105]

Along the PbTe-SnSe quaternary diagonal, we observe relatively asymmetric solubility, with PbTe integrating approximately 60% SnSe ($Pb_{0.4}Sn_{0.6}Te_{0.4}Se_{0.6}$) but SnSe only incorporating 10% of PbTe ($Pb_{0.1}Sn_{0.9}Te_{0.1}Se_{0.9}$). Due to the presence of a three-phase region near the PbTe-SnSe pseudobinary line (discussed later), a routine Vegard's Law analysis is not possible – so we anticipate more error in the solubility limits along this line. Studies along this pseudobinary are not common, but a singular study investigating the PbTe-SnSe phase diagram suggests near identical compositions at decomposition, 61 % PbTe in SnSe and 10 % SnSe in PbTe respectively.[98] Interestingly, both our study and prior literature identify that the phase boundary of SnSe is concave, with the lowest solubility along the diagonal PbTe-SnSe direction.[98] This is unusual, as one would generally expect entropic contributions to extend the solubility along the diagonal.

As the PbTe, PbSe, and SnTe all share the rocksalt phase, we can naively divide the region into "rocksalt" and SnSe. We would expect a minimum of 3 unique regions: 1) single phase rocksalt, 2) two-phase (rocksalt + SnSe), and 3) single phase SnSe. However, our analysis suggests that there appears to be a narrow three-phase region near SnSe. From diffraction and microscopy, it appears that the three-phase region is comprised of two rocksalt phases with differing stoichiometry and SnSe. As this was not explicitly noted in the prior study of the PbTe-SnSe pseudobinary,[98] we performed additional synthesis to ensure that the three-phase region was not caused by our relatively accelerated processing. Several studies were performed using classical synthesis methods and extended annealing times – we note that many samples within the three-phase region revert to two-phase under extended annealing. However, the sample at $Pb_{0.2}Sn_{0.8}Te_{0.3}Se_{0.7}$ remains three-phase. This suggests that the 3-phase region may be thermodynamically robust, although the true composition range is likely smaller than what we observe in the 121 sample grid. This is a key observation, as the most robust 3-phase sample ($Pb_{0.2}Sn_{0.8}Te_{0.3}Se_{0.7}$) is not on the diagonal between PbTe-SnSe, and would not have been investigated in prior studies.[74,98] The single-phase SnSe phase is relatively small, although cell volume shifts within the region are linear and consistent with a Vegard's Law interpretation of alloying.

Throughout the single-phase rocksalt alloy, we note incredibly linear shifts in the cell volume. Even though the volumetric expansion along the PbTe-PbSe edge is nearly twice as strong (-40Å^3) as that observed along the PbTe-SnTe (-17Å^3) or PbSe-SnTe (-23Å^3) edges, the surface formed by the cell volume as a function of composition is very nearly an ideal plane. However, within the two-phase regions, we note relatively different behaviors. Consider the two-phase region adjacent to the SnTe-SnSe pseudobinary – as a consequence of the phase boundary lying along an iso-volumetric contour in the rocksalt phase, the two-phase region demonstrates a near constant cell volume. Contrast this with the two-phase region adjacent to the PbSe-SnSe two-phase region – the extended solubility of SnSe in PbSe forces the phase boundary to cut across the volumetric contours. As a result, the thermodynamic tie lines within the two-phase region generate significant variation in the cell volume.

Speculating, it is possible that the discrepancy between these behaviors is the driving force for the rocksalt miscibility gap (three-phase region). However, we note that the difference between the lattice parameters on either side of the three-phase region is not overly discontinuous. Despite our extended annealing study on ($Pb_{0.2}Sn_{0.8}Te_{0.3}Se_{0.7}$) suggesting that the three-phase region persists after annealing, we remain cautious of kinetic limitations in the multi-phase samples.

Within the single-phase region, the cell volume demonstrates incredibly linear dependencies with the compositional axes – creating a near ideal planar surface. Further, our solubility limits have excellent agreement with literature values.[96–105] Thus, even with our accelerated synthetic throughput, we expect that our single-phase rocksalt and single-phase SnSe regions are representative of bulk polycrystalline samples produced through more traditional means. With alloying confirmed and the phase boundaries understood, we now turn to examine the thermoelectric transport properties within the alloying grid.

3.2 Electronic Transport

We have shown that the alloying properties within the PbTe-PbSe-SnTe-SnSe system are representative of bulk samples in terms of the crystallography and the phase boundaries. However, it is also imperative that thermoelectric transport properties are representative of bulk. Parameters like the electronic mobility, electrical resistivity, and thermal conductivity are intimately connected to scattering (e.g. point defects, grain boundaries) and are good indicators of sample quality. Additionally, as one of the largest agglomerations of experimental data within the PbTe-PbSe-SnTe-SnSe system, we have the opportunity to look for well-known second order effects (e.g. band inversion, point-defect phonon scattering) as a function of chemistry. It is important to stress that this study will be performed at room temperature only – although with a significant time investment high-temperature measurements could be performed as well.

Within this study, the carrier concentration of our binary precursors was not explicitly controlled for *via* extrinsic dopants. However, akin to the concept of phase boundary mapping,[117–120] all precursors were synthesized under chalcogen rich conditions, noted predominately by the appearance of Te or Se within electron microscopy. This generally ties the precursor powders to the p-type (cation-poor) edge of the single phase region. As the fundamental transport parameters (resistivity, Seebeck coefficient) depend intimately on the carrier density, we find it natural to first examine changes in the intrinsic carrier concentration and the resulting effect on resistivity and Seebeck coefficient. Figure 3 shows heat maps of the Hall carrier concentration, electronic resistivity, and Seebeck coefficient for the PbTe-PbSe-SnTe-SnSe system. Note that the raw data for these and additional heat maps (e.g. Hall mobility, Seebeck-derived density of states effective mass) can be found in the ESI, Figures S4-S6.

Within the single-phase rocksalt region, the carrier density (Figure 3a) demonstrates a striking dependence with the Sn content. Alloys between PbTe-SnTe and PbSe-SnTe exhibit near exponential increases (linearly graded colors) in the carrier density with Sn alloying. Interestingly enough, the carrier concentration appears largely invariant with the Te/Se ratio. SnSe shows markedly less variation in the carrier concentration, although the reduced solubility of Pb and Te in SnSe limits our analysis. Note the sharp transition from intrinsic SnSe to degenerate SnTe along the SnSe-SnTe pseudobinary. Presumably we are seeing the effect of percolation, wherein the matrix phase switches from intrinsic SnSe to degenerate SnTe.

We find it fascinating that changes in the Pb/Sn ratio causes such dramatic changes in the carrier concentration within the single-phase rocksalt alloy. The substitution of Pb^{2+} for Sn^{2+} is nominally isoelectronic, and would not be expected to significantly change the carrier concentration on charge counting arguments alone. Thus, we must deduce that the changes in the carrier concentration are associated with fundamental changes in the underlying defect energetics (e.g. vacancies). In the case of Te-rich PbTe, the lowest energy compensating defects are V_{Pb}^{2-} and Te_{Pb}^{2+}.[121–123] The resulting defect equilibria sets Te-rich PbTe as a lightly p-type intrinsic semiconductor. We presume PbSe follows a similar trend, although no robust defect studies within PbSe currently exist. In contrast, SnTe readily forms V_{Sn}^{2-}, leading to degenerate p-type transport.[124–130] Given that PbTe and SnTe share a full solid solution, a strong shift in the native carrier concentration *must* emerge, although this is merely an empirical statement and does not explain the underlying mechanism. Extrapolating from the pure endpoints, it is possible that the compositional shift from Sn to Pb occurs in parallel with changes in an effective "cation-vacancy" formation energy. This would intuitively grade the total vacancy concentration along the alloy, resulting in a smooth transition from intrinsic PbTe to degenerate SnTe, as observed in experiment. Our hypothesis is only a speculation, although we find this topic intriguing, particularly with the lack of defect calculations within heavily alloyed systems. The requisite calculations are outside the scope of this paper, however.

With the general trends in the carrier concentration established, we can turn to examine the electronic resistivity and Seebeck coefficient (Figure 3b and c) within the PbTe-PbSe-SnTe-SnSe alloy. The coupling between the carrier concentration and the electronic resistivity is intuitively the simplest – increases in the carrier concentration will generally yield reduced resistivity. In truth, the resistivity also depends strongly on scattering (point-defect, grain-boundary). Figure 3b shows the heat map of the electronic resistivity throughout the PbTe-PbSe-SnTe-SnSe alloy. First and foremost, we observe remarkably smooth and continuous changes in the resistivity. The continuity of the heat map speaks to the quality and reproducibility of the synthesis method. The trends seen in the resistivity generally mirror the Hall carrier concentration, with the resistivity decreasing near exponentially as we approach SnTe from PbTe and PbSe. Unlike the Hall carrier concentration measurement, however, the resistivity smoothly transitions between the single-phase rocksalt, two/three-phase region, and single-phase SnSe. This is a consequence of the effective media theory and its application to multi-phase transport measurements.

Compared with the electronic resistivity, the Seebeck coefficient (Figure 3c) shows more complex trends. Mathematically, the Seebeck coefficient depends non-monotonically on the carrier density (Fermi level). The Seebeck coefficient is generally very low for heavily doped semiconductors($>10^{20}\,cm^{-3}$) and rises with decreasing carrier concentration until a maximum within the mid 10^{18}–$10^{19}\,cm^{-3}$. Further decreases in the carrier concentration will cause Seebeck to decrease again and eventually switch sign within the bipolar regime. The Seebeck coefficient is also sensitive to the band-gap and changes in the electronic structure (e.g.

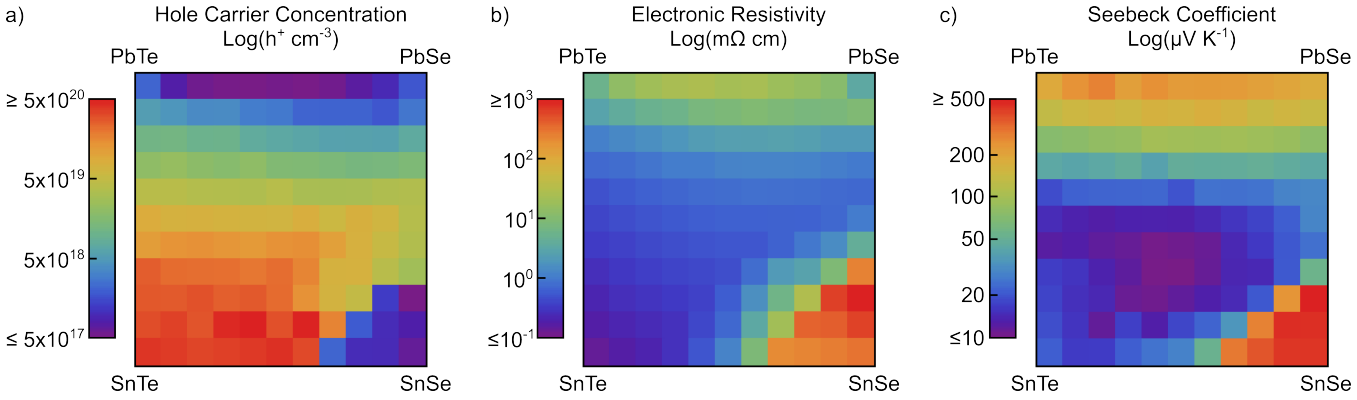

Fig. 3 Hall and Seebeck effect measurements at room temperature on the PbTe-PbSe-SnTe-SnSe alloying system reveal smoothly varying electronic transport as a function of composition. For the pure endpoints and the pseudobinary alloys, results are in excellent agreement with literature.[64,65,67,69,72,74,75,77–79,116] PbTe and PbSe exhibit carrier concentration (a) and electronic resistivity (b) measurements consistent with lightly doped semiconductors. Additionally, our results agree that SnTe is a heavily doped semi-metal and SnSe is intrinsic and resistive. The resistivity varies smoothly and continuously throughout the entire alloying grid, demonstrating high sample quality. We observe that the carrier concentration within the rocksalt phase depends heavily on the Sn content, with free carrier concentrations varying over 3 orders of magnitude in what are nominally isoelectronic alloys. Consistent with literature, SnSe remains intrinsic over the single-phase region. The Seebeck coefficient (c) is particularly interesting as it convolutes changes in the carrier concentration and the underlying electronic structure. The anomalous "pocket" of low Seebeck coefficient may indicate an extended region of band inversion.

density of states effective mass, band degeneracy). Within our experimental data, the Seebeck coefficient broadly shows the convolution of two effects: changes in carrier density and emergence of band inversion. Examining the changes in carrier density first, we note that the Pb-rich compositions have Seebeck coefficients that strongly depend on the Sn content and are largely invariant of the Te/Se ratio. This is conceptually consistent with the changes in the carrier concentration and the expected dependence of the Seebeck coefficient on the Fermi level. However, the invariance in the Te/Se ratio also suggests that there are not significant changes in the valence band density of states effective mass with alloying. These trends would likely evolve with temperature, as there are well noted instances of band convergence along the PbTe-PbSe alloys at high-temperature.[64] Where available, our Seebeck S and resistivity ρ values yield power factor calculations ($PF = S^2/\rho$) in good agreement with the literature.[65,68,74,75,79,131] Some variation is noted, although this is likely due to differences in carrier concentration, as our materials were not intentionally doped.

At the Sn-rich compositions, we observe that the Seebeck coefficient dips into a "pocket" ($<10\,\mu$V/K) near the middle of the heat map. This trend is not consistent with changes in the carrier concentration. Consider the PbTe-SnTe pseudobinary. Starting at PbTe, the Seebeck coefficient decreases with Sn substitution (consistent with carrier concentration) until it reaches a minimum at approximately 60% SnTe. Although the carrier concentration continues to increase as we approach pure SnTe, the Seebeck coefficient actually recovers. This effect is consistent with the concept of "band inversion" noted in the literature. In fact, prior literature quotes that 62-67 % SnTe is the critical composition where band inversion occurs at room temperature.[132–134] Prior literature also demonstrates band inversion in the PbSe-SnSe alloy at low temperatures.[82] Our literature survey reveals a surprising lack of papers along the PbSe-SnTe pseudobinary, although one should naturally expect band inversion to occur there as well.

While not directly pertinent to thermoelectric performance, band inversion in the PbTe-SnTe alloys is of interest as a topological crystalline insulator.[84,135–137] The effect is a fascinating manifestation of band structure evolution with alloying and the emergence of purely quantum mechanical effects. Band inversion emerges because PbTe and PbSe have a direct gap at the L-point which is comprised of a valence band maximum with L_6^+ symmetry and a conduction band minimum with L_6^- symmetry. In SnTe, the band natures are reversed. The reversal, known as "Dimmock reversal" occurs due to the relativistic nature of the Pb atom and strong s-p coupling in SnTe.[132,138] Alloys between structures with different band characters experience a transition point where the valence band switches from L_6^+ to L_6^-, causing a intermediate composition where the band gap collapses, the dispersion appears Dirac-like, and topological insulating behavior can be observed.[132,133,135,136,139]

Within our alloying study, we actually observe a wide range of compositions that exhibit anomalously reduced Seebeck coefficients. This suggests that there may be an array of compositions within the PbTe-PbSe-SnTe-SnSe alloys that exhibit band inversion. Considering that the band inversion also appears to vary strongly with temperature,[82] there appears to be a significant amount of tunability in both the composition and temperature dimensions – an interesting case which may deserve a HTP study in itself, particularly if we invoke extrinsic dopants as well. In this work, we use the Seebeck coefficient as a proxy for the band inversion, though optical or ARPES measurements could confirm the extended region of band inversion. These studies are outside the scope of this work, but the mere identification of these potential follow-up studies continues to prove HTP experiment as a powerful screening and exploration tool.

All of the prior measurements depend intimately on the carrier concentration, although we mentioned that the resistivity also depends critically on scattering phenomena and the underlying elec-

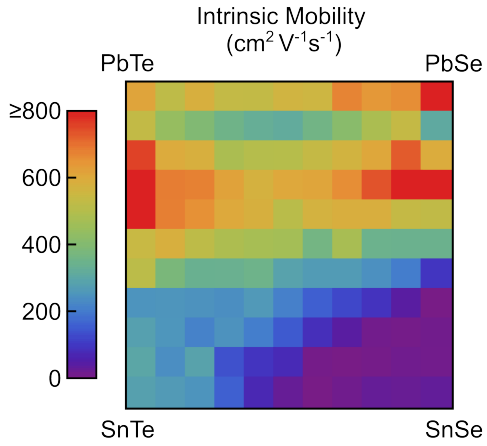

Fig. 4 To decouple the effect of carrier concentration from the electronic mobility, we used the single-parabolic (SPB) model to extract the intrinsic mobility. While alloying is generally expected to reduce the intrinsic mobility, we note several regions where high electronic mobility is preserved. Note that the phenomenon of band-inversion is well documented around 60% SnTe, and may play a significant role in the mobility changes along this edge (e.g. band shape transition from parabolic to Kane-like to Dirac-like).

tronic structure. The natural metric for examining these effects in alloys is the electronic mobility, although the strong changes in carrier concentration make it difficult to decouple changes in scattering, electronic structure, and carrier density. A convenient workaround is to extract the "intrinsic mobility." Under the single parabolic band (SPB) model, the experimental Seebeck coefficient S can be used to extract the electron chemical potential (η) by solving Equation 1 for η:

$$S(\eta) = \frac{k_b}{e}\frac{(2+\lambda)F_{1+\lambda}(\eta)}{(1+\lambda)F_{\lambda}(\eta)} - \eta \quad (1)$$

The chemical potential can then be combined with the experimental Hall mobility to estimate the intrinsic mobility μ_0 (Equation 2):

$$\mu_0 = \mu_{\text{Hall}}\frac{2}{\sqrt{\pi}}\frac{\Gamma_{1+\lambda}F_{0.5}(\eta)}{F_{\lambda}(\eta)} \quad (2)$$

where Γ is the gamma function, F is the Fermi integral, and λ is a scattering dependent parameter. We assume all materials are dominated by acoustic phonon scattering, which yields $\lambda = 0$. Although the process carries several assumptions (single parabolic band, acoustic phonon scattering, no bipolar contribution), it is a commonly used approximation in thermoelectrics as a way to make model-consistent comparisons between systems. Figure 4 shows the SPB derived intrinsic mobility within the PbTe-PbSe-SnTe-SnSe alloying plane. Note that the data used to generate Figure 4 and the underlying Hall mobility can be found in the ESI, Figure S7 and S8.

The intrinsic mobility exhibits several interesting trends. Naively, we would expect the mobility to decay with increased alloying due to increased point-defect (alloy) scattering. Instead, we see pockets of relatively high mobility material within the intermediate alloys. Two distinct regions appear: one on the PbTe-SnTe pseudobinary and another near the PbSe-SnSe pseudobinary. The endpoints (e.g. PbSe) also appear to be high mobility, as one would expect. Particularly along the PbTe-SnTe pseudobinary, we are curious as to whether the band inversion plays a significant role in the increased mobility. From literature, the band inversion between PbTe-SnTe generally occurs near 60% SnTe,[132,133,139] although the maxima in our intrinsic mobility appears around 30-40% SnTe. However, as we near the inversion, we could reasonably expect the nature of the band edges to shift from parabolic to Kane-like (eventually ending in Dirac-like at the inversion). This would significantly decrease the band effective mass and potentially increase the electronic mobility. Interestingly enough, we do seem to note a transition around 60% SnTe, past which the intrinsic mobility appears significantly reduced. To supplement the intrinsic mobility data, we have also included a table of the Seebeck-derived density of states effective mass for each sample (see ESI, Figure S9).

It is interesting that prior studies along the PbTe-SnTe pseudobinary did not identify a region of increased mobility. However, the prior literature has historically used the raw Hall mobility and does not correct to the carrier concentration independent intrinsic mobility.[81,116] Thus, prior work may have been unable to resolve a relatively subtle increase in the intrinsic mobility from the strong (order of magnitude) changes in the carrier concentration. We also note that the intrinsic mobility will evolve substantially with temperature, and while high-temperature measurements were outside the scope of this work, they would assuredly produce an even richer understanding of the underlying transport.

Even at room-temperature, the electronic measurements of our 121 sample grid have produced a rich dataset. We have simultaneously discovered several interesting trends (e.g. band inversion, high-mobility alloys, Sn-doping of PbTe) while simultaneously recreating a plethora of historical alloying data. While much of this work is preliminary, it exemplifies the power of HTP experimental methods. The high-mobility alloys are of particular interest for thermoelectrics. However, we are careful to note that the electronic mobility and thermal conductivity (and ultimately zT) are rarely optimized at the same composition. As such, the next section focuses on the thermal transport within the PbTe-PbSe-SnTe-SnSe system.

3.3 Thermal Transport

Within thermoelecrics, alloying is perhaps *the* most common technique used when manipulating the thermal conductivity. Indeed, many high-performance PbTe-based thermoelectric materials are heavily alloyed.[67,140–142] The theory of point-defect (alloy) scattering and the effect on the lattice thermal conductivity has been well studied in the literature. Multiple models have been presented, many of which are based on a combination of geometric factors (e.g. ionic radii, bond distortion) and mass contrast.[143–147] All results generally imply that the lattice thermal conductivity should decrease with alloying, resulting in a minimum vaguely near the center of the solid solution. This logic is the basis for the "high-entropy" alloying studies within PbTe, which are some of the only papers to investigate the properties

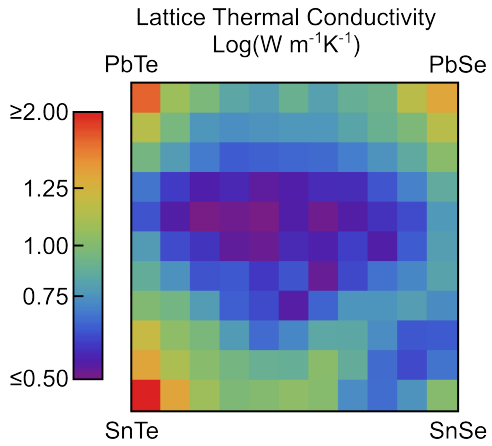

Fig. 5 Consistent with historical and conceptual models of point-defect (alloy) scattering, the thermal conductivity decreases with increased alloying. This naturally yields a wide region of low lattice thermal conductivity which is concentrated near the center of the alloying grid. At room temperature, we note that the thermal conductivity exhibits very low values ($<0.5\,W\,m^{-1}\,K^{-1}$) over a relatively wide range of compositions. Notably, the lowest values do *not* coincide with the center of the plot ($Pb_{0.5}Sn_{0.5}Te_{0.5}Se_{0.5}$).

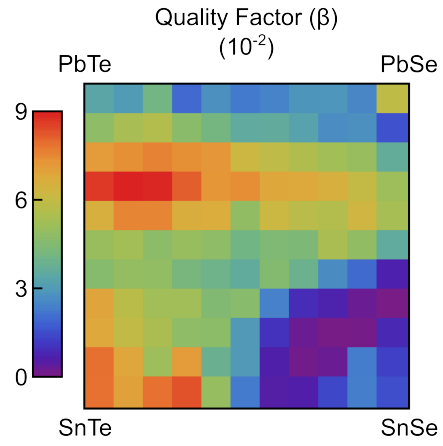

Fig. 6 The thermoelectric quality factor β serves as a carrier concentration-independent proxy for the figure of merit zT. As β convolutes the trends seen in the lattice thermal conductivity and intrinsic mobility, we can see that the optimal composition is neither at the maximum intrinsic mobility nor the minimum lattice thermal conductivity. While this study did not include doping or temperature-based effects, it still shows that the optimal composition may not lie upon the intuitive compositions (e.g. psuedobinaries, high-entropy mixtures).

away from the pseudobinary edges of the phase diagram.[66,74]

To investigate the effect of point-defect scattering on the lattice thermal conductivity, we first correct the total thermal conductivity using a Lorenz correction for the electronic thermal conductivity. As a wide variety of carrier concentrations are observed in the dataset, the Lorenz number is calculated using the experimentally observed Seebeck coefficient. The resulting lattice thermal conductivity heat map is shown in Figure 5. The data used to generate Figure 5, including the total thermal conductivity map, is included in the ESI, Figures S10 and S11.

As expected, we generally observe depressions in the lattice thermal conductivity with increased alloying. We find it interesting, however, that there is actually a basin of low values over a wide breadth of compositions. Compared to the pure endpoints, the depth of the basin is quite significant, with a factor 3-4× decrease in the thermal conductivity with alloying. However, as we noted in the previous section, the composition with the lowest thermal conductivity often also exhibits reduced mobility. As such, we must integrate a metric that accounts for simultaneous changes in both the lattice thermal conductivity and the intrinsic mobility. The next section focuses on the *quality factor* β, which allows us to identify promising compositions from their intrinsic (concentration independent) properties.

3.4 Quality Factor β

Historically, the thermoelectric figure of merit (zT) has been the dominant parameter for characterizing the quality of a thermoelectric material. However, zT is implicitly dependent on the carrier concentration and explicitly dependent on the temperature. As such, an optimization of zT requires both doping and high-temperature studies. A full survey of the PbTe-PbSe-SnTe-SnSe space that includes alloying, doping, and temperature would be an exceptionally high-dimensional study. Creating such a study would be a revolutionary endeavour, but it requires additional engineering, visualization, and synthetic considerations which are outside the scope of this pilot study – however, we believe that the experimental techniques to create bulk samples at this scale are not out of reach.

In the absence of zT, we can apply another historical metric for thermoelectric performance, the thermoelectric quality factor β.[29,148,149] Unlike zT, β is a carrier concentration independent parameter, although it assumes that the optimal carrier concentration can ultimately be achieved. Under this assumption, β convolutes the lattice thermal conductivity, intrinsic mobility, and Seebeck effective masses to provide a measure of ultimate thermoelectric performance under ideal doping conditions. Figure 6 shows our calculation of β across our alloying study. The data used to generate Figure 6 can be found in the ESI, Figure S12.

The quality factor β is useful in that it mathematically convolutes the changes in the lattice thermal conductivity, intrinsic mobility, and Seebeck effective mass. Due to the complex interplay between the thermoelectric transport coefficients, the composition for optimal performance rarely coincides with the extrema of any given coefficient. We can see this quite clearly in Figure 6. The intrinsic mobility had a local maximum along the PbTe-SnSe pseudobinary around 30-40% SnTe, whereas the lattice thermal conductivity generally shows a minimum closer to the center of the diagram. The confluence of these effects "pulls" the high β sample off of the pseudobinary PbTe-SnTe line. Furthermore, the highest β composition ($Pb_{0.7}Sn_{0.3}Te_{0.9}Se_{0.1}$) does not lie along any intuitive set of compositions (e.g. diagonals, edges, center).

Even without high-temperature measurements or extensive doping studies, this work already demonstrates that high-dimensional optimization within material science may elude chemical intuition. Considering that the optimization of β in Figure 6 will likely evolve with temperature, the search for the global

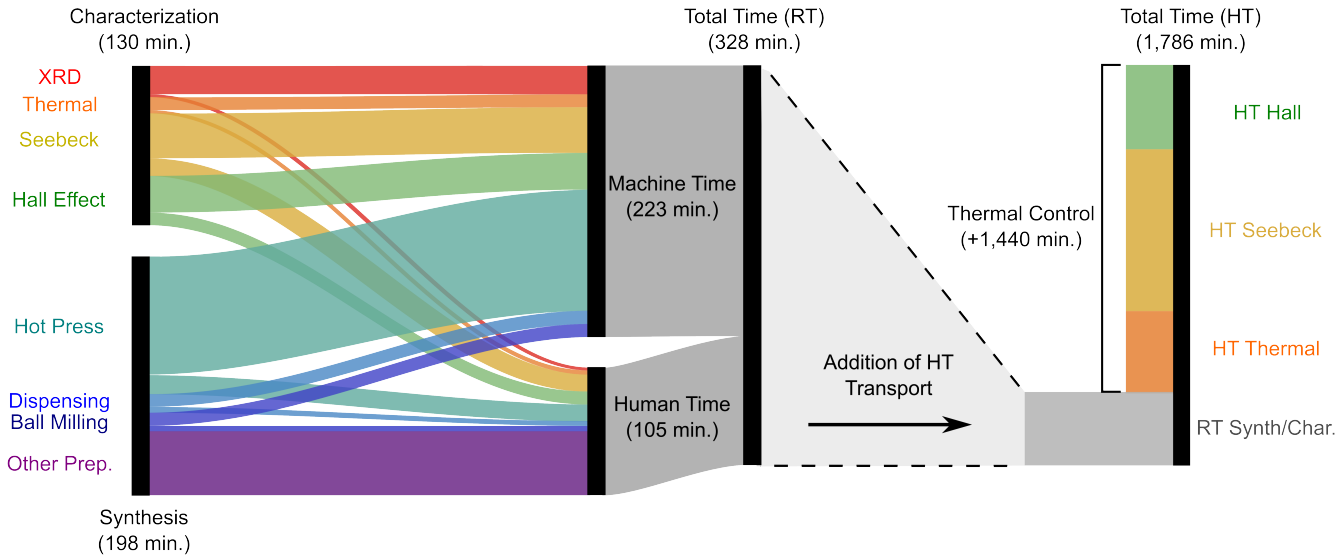

Fig. 7 Sankey plot demonstrating the time investment required (per sample) throughout this work. At room-temperature, the synthesis time is moderately larger (198 min) than the characterization time (130 min). To investigate individual contributions, we can subdivide the characterization and synthesis times into technique-specific time allotments (colored) and further into "machine time" and "human time" specific processes. We propose using parallelization to alleviate "machine time" intensive processes while increasing automation to reduce "human time." As constructed, this plot is a pilot case for the use of HTP synthesis and characterization as a means to screen for effective compositions. While high-temperature and HTP methods are the ultimate goal, an addendum to the Sankey diagram (right, light gray) demonstrates the large increase in time associated with performing subsequent high-temperature measurements. Overcoming this bottleneck will require significant time and capital investment.

maxima within PbSnTeSe would be a daunting task using classical methods. While not impossible via intuition alone, the addition of HTP tools would dramatically augment our experimental prowess and accelerate the optimization of new materials.

3.5 Future of High-Throughput

Our study within the PbTe-PbSe-SnTe-SnSe systems has clearly demonstrated that HTP synthesis is a worthwhile endeavour. Even within this pilot study, we have replicated >50 years of PbTe-PbSe-SnTe-SnSe alloying studies while simultaneously revealing new trends. Besides dramatically increasing the rate of optimization and discovery of new materials, HTP experiment would also radically improve synergy with existing computational and theoretical efforts. The high-dimensional data sets would also provide powerful techniques like machine learning and data-driven experimental design to generate new models and guide our insight into complex optimization problems.

Our work thus far has provided a glimpse of the value that HTP experiment can provide. However, this work was still a time-intensive and effort-intensive process. Future development of HTP experiment (particularly with a focus on automation or parallelization) will want to direct additional engineering efforts to expedite the most time-consuming processes. This is particularly true if the complexity of the synthesis increases (e.g. including multiple dopants, changing processing conditions) or if higher resolution maps are desired (e.g. 1-5% alloying steps). Throughout the synthesis and characterization of our 121 sample PbTe-PbSe-SnTe-SnSe alloying map, we gathered a significant amount of metadata quantifying time expenditure per sample and per process. The purpose of this section is to investigate this data from an engineering perspective – to identify bottlenecks and discuss potential solutions. We will not discuss financial costs (e.g. material costs, labor costs) within this work, as proposed solutions are currently speculative.

In the context of our experiment, we want to examine how time is invested during the synthesis and characterization of a sample. Figure 7 visualizes the time allocation metadata as a Sankey diagram. Sankey diagrams are representations of resource flow binned to demonstrate resource allocation and subdivision. On Figure 7, each black bar indicates a general "pool" of allocated time, and the colored subdivisions show how each "pool" is divided into process-specific subsystems. Each process-specific cost (colored) is further subdivided into "machine time" and "human time." As we use it, machine time is defined as any period of time where an instrument is running but *a human is not required to be present*. Human time specifically requires a human to be present and physically engaged with the sample or instrument. This is an incredibly important division, as it broadly defines how to adapt the technique to HTP studies. Techniques that predominantly consume machine time can be expedited by parallelization, whereas human time is alleviated through automation. This paper only enumerates the synthesis and room-temperature measurements in detail, although we also consider the (time) cost of high-temperature characterization.

Sankey diagrams are relatively complex representations of data, so it helps to have specific goals when reading one. Figure 7 is constructed explicitly to provide guidance when asking future-looking engineering questions:

1. Which is more prohibitive, synthesis or characterization?
2. Which technique is the most time consuming, and can we triage techniques based on time consumption?
3. Should we preferentially improve techniques which consume more human time?

By understanding the answers to these questions, we will be better equipped to design HTP systems that address tangible bottlenecks.

Which is more prohibitive, synthesis or characterization? This is actually a nuanced question, as the answer depends dramatically on whether or not we consider high-temperature measurements. Looking at the leftmost black bars on Figure 7, we can see that synthesis (198 min/sample) is slightly more time consuming that characterization (130 min/sample) when only room-temperature measurements are invoked. This is a relatively large improvement over our classical techniques, as synthesis has been hastened by a factor of 3-5×. Furthermore, when the synthesis and characterization times are roughly matched, the whole process can theoretically proceed at steady-state, with no accumulation of uncharacterized samples or downtime of characterization instruments. However, if we include high-temperature measurements (right side of Figure 7), we can see that characterization is now an overwhelmingly costly venture. Currently, integration of high-temperature measurements at large scale is not viable, nor are there currently available commercial systems that can perform HTP high-temperature measurements. Thus, implementation of high-temperature HTP measurements represents a significant engineering challenge that must be contended with as synthetic approaches continue to accelerate.

Which technique is the most time consuming, and can we triage techniques based on time consumption? As mentioned in the previous discussion, high-temperature HTP characterization is definitely a subject deserving of attention. However, there alternative ways of viewing the problem. If high-temperature HTP characterization is not available, we can still use room-temperature measurements to screen for effective compositions. In this situation, we would want to continue to reduce synthesis times to align with the room-temperature characterization time. Looking at the most time-consuming processes, we see that hot pressing and sample preparation are the dominant contributors to the synthesis time. As hot pressing is predominantly a "machine time" intensive process, we would want to continue increasing parallelization efforts. Sample preparation is predominantly associated with cleaning, polishing, thickness, and density measurements. All of these techniques can be expedited by transforming them into "machine time" processes *via* automation (e.g. autopolisher, gas pycnometer). Interestingly enough, as synthesis methods quicken, we will inherently need to explore improvements to the room-temperature characterization processes as well.

Should we preferentially improve techniques which consume more human time? This problem is not easily answered. From a throughput perspective, the least efficient tasks should be improved upon first, as they will likely lead to the largest improvement in performance. However, without invoking full automation and characterization, we must also consider the human element of the equation. Consider the "human time" associated with the four characterization techniques. This time is entirely associated with sample loading/unloading from individual systems. Practically, each task only takes a few minutes, but maintaining a steady flow of samples through the characterization systems is exhausting and requires continuous multitasking – preventing the researcher from investing time elsewhere. By automating and integrating the different characterization techniques into a singular instrument, samples could be loaded in batches, allowing "human time" to be better spent elsewhere. Ironically, even though human-time is not a overwhelmingly large component of the characterization and synthesis processes, any improvements which reduce rote tasks may result in disproportionately large improvements in throughput. We suspect that this discussion resonates even more deeply when financial considerations (e.g. wages) are taken into account.

Naively, we expected that Figure 7 would allow us to identify a singular, key obstacle to the continued improvement of HTP synthesis and characterization. Instead, it presented a relatively nuanced representation of a complex problem. We can expedite synthesis by further parallelization of hot pressing and automation of sample preparation, although at some point we will generate samples faster than they can be measured. We can automate the process of room-temperature measurements through a custom-built characterization system, but high-temperature measurements will still represent a significant bottleneck. We need to decide whether the ultimate goal is to simply eliminate actions which are "human time" costly, or to increase throughput in a holistic sense. Ultimately we conclude that realization of a true HTP synthesis and characterization setup will require simultaneous investment in automation and parallelization. High-temperature measurements must also be considered, as thermoelectric performance commonly requires high-temperature characterization (exception being refrigeration). Reductions in "human time" must be balanced with financial and "machine time" costs. This work has been explicitly framed within thermoelectrics, although we expect that the fundamental concepts will resonate within other fields of material science as well.

4 Conclusion

When we began this work, we had three primary goals: 1) provide proof of concept that HTP bulk synthesis can add value to experimental studies, 2) identify where additional engineering can ameliorate potential bottlenecks, and 3) investigate fundamental material science within some of the most industrially relevant thermoelectric compounds.

By adapting classical synthesis methods towards HTP ideology, we created the largest bulk investigation into the PbTe-PbSe-SnTe-SnSe alloy system to date. Not only were we able to recreate over 50 years of alloying literature and phase diagram data, but we also identified new trends (e.g. wide range of band inversion, high mobility alloys). This work highlights that chemically intuitive compositions are not guaranteed to capture anomalous trends, particularly when the application space is complex and high-dimensional. HTP synthesis and characterization tech-

niques are uniquely suited to screening wide chemical spaces, and the integration of modern technologies (automation, data-driven methodologies) would allow for rapid development of new materials with intuition-agnostic search strategies.

Our analysis also provided guides for future HTP efforts. Simultaneous automation and parallelization will be required to hit throughput goals, particularly if high-temperature characterization is included. However, despite remaining challenges, we are convinced that the means to create a fully HTP experimental setup is within reach. With continued focus on production of high-quality bulk samples, the integration of HTP methodologies has the potential to revolutionize the field of material science.

5 Conflicts of Interest

There are no conflicts of interest to declare.

6 Acknowledgements

This work was funded by the National Science Foundation (NSF) DMREF program 1555340. This work was also funded by the U.S. Department of Energy, ARPA-E IDEAS program 1428-1737.

References

1 Z. Deng, F. Wei, S. Sun, G. Kieslich, A. K. Cheetham and P. D. Bristowe, J. Mater. Chem. A, 2016, **4**, 12025–12029.
2 L. Yu and A. Zunger, Phys. Rev. Lett., 2012, **108**, 068701(1)–068701(5).
3 A. Zakutayev, J. Mater. Chem. A, 2016, **4**, 6742–6754.
4 K. B. Ørnsø, J. M. Garcia-Lastra and K. S. Thygesen, Phys. Chem. Chem. Phys., 2013, **15**, 19478–19486.
5 I. Y. Kanal, S. G. Owens, J. S. Bechtel and G. R. Hutchison, J. Phys. Chem. Lett., 2013, **4**, 1613–1623.
6 E. Mosconi, A. Amat, M. K. Nazeeruddin, M. GraÌĺtzel and F. De Angelis, J. Phys. Chem. C., 2013, **117**, 13902–13913.
7 I. E. Castelli, T. Olsen, S. Datta, D. D. Landis, S. Dahl, K. S. Thygesen and K. W. Jacobsen, Energy. Environ. Sci., 2012, **5**, 5814–5819.
8 J. K. Nørskov, T. Bligaard, J. Rossmeisl and C. H. Christensen, Nat. Chem., 2009, **1**, 37–46.
9 M. P. Andersson, T. Bligaard, A. Kustov, K. E. Larsen, J. Greeley, T. Johannessen, C. H. Christensen and J. K. Nørskov, J. Catal., 2006, **239**, 501–506.
10 S. Linic, J. Jankowiak and M. A. Barteau, J. Catal., 2004, **224**, 489–493.
11 P. Strasser, Q. Fan, M. Devenney, W. H. Weinberg, P. Liu and J. K. Nørskov, J. Phys. Chem. B, 2003, **107**, 11013–11021.
12 J. Sehested, K. Larsen, A. Kustov, A. Frey, T. Johannessen, T. Bligaard, M. Andersson, J. Nørskov and C. Christensen, Top. Catal., 2007, **45**, 9–13.
13 J. K. Nørskov, F. Abild-Pedersen, F. Studt and T. Bligaard, Proc. Natl. Acad. Sci. U.S.A., 2011, **108**, 937–943.
14 J. Greeley and M. Mavrikakis, Nat. Mater., 2004, **3**, 810–815.
15 J. L. Spivack, J. N. Cawse, D. W. Whisenhunt, B. F. Johnson, K. V. Shalyaev, J. Male, E. J. Pressman, J. Y. Ofori, G. L. Soloveichik, B. P. Patel, T. L. Chuck, D. J. Smith, T. M. Jordan, M. R. Brennan, R. J. Kilmer and E. D. Williams, Appl. Catal., A, 2003, **254**, 5–25.
16 X. Qu, A. Jain, N. N. Rajput, L. Cheng, Y. Zhang, S. P. Ong, M. Brafman, E. Maginn, L. A. Curtiss and K. A. Persson, Comput. Mater. Sci., 2015, **103**, 56–67.
17 T. Mueller, G. Hautier, A. Jain and G. Ceder, Chem. Mater., 2011, **23**, 3854–3862.
18 A. Jain, G. Hautier, C. Morre, K. Kang Byoungwoo, J. Lee, H. Chen, N. Twu and G. Ceder, J. Electrochem. Soc., 2012, **159**, 622–633.
19 G. Hautier, A. Jain, H. Chen, C. Moore, O. S. Ping and G. Ceder, J. Mater. Chem., 2011, **21**, 17147–17153.
20 G. Hautier, A. Jain, S. P. Ong, B. Kang, C. Moore, R. Doe and G. Ceder, Chem. Mater., 2011, **23**, 3495–3508.
21 F. Zhou, M. Cococcioni, C. A. Marianetti, D. Morgan and G. Ceder, Phys. Rev. B, 2004, **70**, 235121(1)–235121(8).
22 G. Ceder, MRS Bull., 2010, **35**, 693–701.
23 G. K. Madsen, J. Am. Chem. Soc., 2006, **128**, 12140–12146.
24 D. Broido, M. Malorny, G. Birner, N. Mingo and D. Stewart, Appl. Phys. Lett., 2007, **91**, 231922(1)–231922(3).
25 S. Wang, Z. Wang, W. Setyawan, N. Mingo and S. Curtarolo, Phys. Rev. X, 2011, **1**, 021012(1)–021012(8).
26 J. Shiomi, K. Esfarjani and G. Chen, Phys. Rev. B, 2011, **84**, 104302(1)–104302(9).
27 P. Gorai, D. Gao, B. Ortiz, S. Miller, S. A. Barnett, T. Mason, Q. Lv, V. Stevanović and E. S. Toberer, Comput. Mater. Sci., 2016, **112**, 368–376.
28 J. Yang, H. Li, T. Wu, W. Zhang, L. Chen and J. Yang, Adv. Funct. Mater., 2008, **18**, 2880–2888.
29 J. Yan, P. Gorai, B. R. Ortiz, S. Miller, S. A. Barnett, T. Mason, V. Stevanović and E. S. Toberer, Energy Environ. Sci., 2015, **8**, 983–994.
30 J. J. Hanak, J. Mater. Sci., 1970, **5**, 964–971.
31 A. N. Fioretti, A. Zakutayev, H. Moutinho, C. Melamed, J. D. Perkins, A. G. Norman, M. Al-Jassim, E. S. Toberer and A. C. Tamboli, J. Mater. Chem. C, 2015, **3**, 11017–11028.
32 B. Jandeleit, D. J. Schaefer, T. S. Powers, H. W. Turner and W. H. Weinberg, Angew. Chem., 1999, **38**, 2494–2532.
33 M. Watanabe, T. Kita, T. Fukumura, A. Ohtomo, K. Ueno and M. Kawasaki, Appl. Surf. Sci., 2007, **254**, 777–780.
34 M. Watanabe, T. Kita, T. Fukumura, A. Ohtomo, K. Ueno and M. Kawasaki, J. Comb. Chem., 2008, **10**, 175–178.
35 X.-D. Xiang, Mater. Sci. Eng., B, 1998, **56**, 246–250.
36 P. P. Rajbhandari, A. Bikowski, J. D. Perkins, T. P. Dhakal and A. Zakutayev, Sol. Energy Mater. Sol. Cells, 2017, **159**, 219–226.
37 R. Potyrailo, K. Rajan, K. Stoewe, I. Takeuchi, B. Chisholm and H. Lam, ACS Comb. Sci., 2011, **13**, 579–633.
38 M. Otani, N. D. Lowhorn, P. K. Schenck, W. Wong-Ng, M. L. Green, K. Itaka and H. Koinuma, Appl. Phys. Lett., 2007, **91**, 132102(1)–132102(3).
39 M. Otani, K. Itaka, W. Wong-Ng, P. Schenck and H. Koinuma, Appl. Surf. Sci., 2007, **254**, 765–767.
40 D. Music, R. W. Geyer and M. Hans, J. Appl. Phys., 2016,

120, 045104(1)–045104(7).
41 S. S. Mao, J. Cryst. Growth, 2013, **379**, 123–130.
42 M. S. Beal, B. E. Hayden, T. Le Gall, C. E. Lee, X. Lu, M. Mirsaneh, C. Mormiche, D. Pasero, D. C. A. Smith, A. Weld, C. Yada and S. Yokoishi, ACS Comb. Sci., 2011, **13**, 375–381.
43 X. Gong, S. Mohan, M. Mendoza, A. Gray, P. Collins and S. R. Kalidindi, Integ. Mater. Manuf. Innov., 2017, **6**, 218–228.
44 T. A. Stegk, R. Janssen and G. A. Schneider, J. Comb. Chem, 2008, **10**, 274–279.
45 B. C. Salzbrenner, J. M. Rodelas, J. D. Madison, B. H. Jared, L. P. Swiler, Y.-L. Shen and B. L. Boyce, J. Mater. Process. Technol., 2017, **241**, 1–12.
46 Z. Li, A. Ludwig, A. Savan, H. Springer and D. Raabe, J. Mater. Res, 2018, 1–14.
47 H. Springer and D. Raabe, Acta Mater., 2012, **60**, 4950–4959.
48 J. García-Cañadas, N. J. E. Adkins, S. McCain, B. Hauptstein, A. Brew, D. J. Jarvis and G. Min, ACS Comb. Sci., 2016, **18**, 314–319.
49 R. C. Pullar, ACS Comb. Sci., 2012, **14**, 425–433.
50 I. V. Khodyuk, S. A. Messina, T. J. Hayden, E. D. Bourret and G. A. Bizarri, J. Appl. Phys., 2015, **118**, 084901(1)–084901(7).
51 S. Curtarolo, G. L. Hart, M. B. Nardelli, N. Mingo, S. Sanvito and O. Levy, Nat. Mater., 2013, **12**, 191–201.
52 M. L. Green, C. Choi, J. Hattrick-Simpers, A. Joshi, I. Takeuchi, S. Barron, E. Campo, T. Chiang, S. Empedocles, J. M. Gregoire, A. G. Kusne, J. Martin, A. Mehta, K. Persson, Z. Trautt, J. VanDuren and A. Zakutayev, Appl. Phys. Rev., 2017, **4**, 011105(1)–011105(18).
53 J.-F. Li, W.-S. Liu, L.-D. Zhao and M. Zhou, NPG Asia Mater., 2010, **2**, 152–158.
54 J. P. Heremans, C. M. Thrush and D. T. Morelli, Phys. Rev. B, 2004, **70**, 115334(1)–115334(5).
55 B. Poudel, Q. Hao, Y. Ma, Y. Lan, A. Minnich, B. Yu, X. Yan, D. Wang, A. Muto, D. Vashaee et al., Science, 2008, **320**, 634–638.
56 D.-Y. Chung, T. Hogan, P. Brazis, M. Rocci-Lane, C. Kannewurf, M. Bastea, C. Uher and M. G. Kanatzidis, Science, 2000, **287**, 1024–1027.
57 X. Wang, H. Lee, Y. Lan, G. Zhu, G. Joshi, D. Wang, J. Yang, A. Muto, M. Tang, J. Klatsky et al., Applied Physics Letters, 2008, **93**, 193121(1)–193121(3).
58 G. Joshi, H. Lee, Y. Lan, X. Wang, G. Zhu, D. Wang, R. W. Gould, D. C. Cuff, M. Y. Tang, M. S. Dresselhaus et al., Nano Lett., 2008, **8**, 4670–4674.
59 G. Tan, F. Shi, S. Hao, L.-D. Zhao, H. Chi, X. Zhang, C. Uher, C. Wolverton, V. P. Dravid and M. G. Kanatzidis, Nat. Commun., 2016, **7**, 12167.
60 T. Mori, Small, 2017, **13**, 1702013(1)–1702013(10).
61 G. Tan, L.-D. Zhao and M. G. Kanatzidis, Chemical reviews, 2016, **116**, 12123–12149.
62 M. I. Fedorov, M. V. Vedernikov, E. A. Gurieva, L. V. Prokof'eva and Y. I. Ravich, 20th International Conference on Thermoelectrics, 2001, pp. 139–142.
63 G. M. Guttmann, D. Dadon and Y. Gelbstein, Journal of Applied Physics, 2015, **118**, 065102(1)–065102(6).
64 Y. Pei, X. Shi, A. LaLonde, H. Wang, L. Chen and G. Jeffrey Snyder, Nature, 2011, **473**, 66–69.
65 L. P. Tan, T. Sun, S. Fan, R. V. Ramanujan and H. H. Hng, J. Alloys Compd., 2014, **587**, 420–427.
66 Z. Fan, H. Wang, Y. Wu, X. Liu and Z. Lu, Mater. Res. Lett., 2017, 1–8.
67 I. Kudman, J. Mater. Sci., 1972, **7**, 1027–1029.
68 Q. Zhang, F. Cao, W. Liu, K. Lukas, B. Yu, S. Chen, C. Opeil, D. Broido, G. Chen and Z. Ren, J. Am. Chem. Soc., 2012, **134**, 10031–10038.
69 T.-R. Wei, G. Tan, C.-F. Wu, C. Chang, L.-D. Zhao, J.-F. Li, G. J. Snyder and M. G. Kanatzidis, Appl. Phys. Lett., 2017, **110**, 053901(1)–053901(5).
70 A. Bali, H. Wang, G. Snyder and R. C. Mallik, J. Appl. Phys., 2014, **116**, 033707(1)–033707(7).
71 V. Jovovic, S. J. Thiagarajan, J. P. Heremans, T. Komissarova, D. Khokhlov and A. Nicorici, J. Appl.Phys., 2008, **103**, 053710(1)–053710(7).
72 A. Banik and K. Biswas, J. Mater. Chem. A, 2014, **2**, 9620–9625.
73 J. Cui, X. Qian and X. B Zhao, J. Alloys Compd., 2003, **358**, 228–234.
74 B.-C. Qin, Y. Xiao, Y.-M. Zhou and L.-D. Zhao, Rare Metals, 2018, **37**, 343–350.
75 C.-F. Wu, T.-R. Wei and J.-F. Li, Phys. Chem. Chem. Phys., 2015, **17**, 13006–13012.
76 P. M. Nikolic, Br. J. Appl. Phys., 1965, **16**, 1075–1079.
77 C. M. Jaworski, B. Wiendlocha, V. Jovovic and J. P. Heremans, Energy Environ. Sci., 2011, **4**, 4155–4162.
78 M. Orihashi, Y. Noda, L.-D. Chen, T. Goto and T. Hirai, J. Phys. Chem. Solids, 2000, **61**, 919–923.
79 Y. Gelbstein, Z. Dashevsky, Y. George and M. P. Dariel, 25th International Conference on Thermoelectrics, 2006, pp. 79–80.
80 V. Markov, N. Tretyakova, L. Maskaeva, V. Bakanov and H. Mukhamedzyanov, Thin Solid Films, 2012, **520**, 5227–5231.
81 A. Toneva and A. Alazhazhian, Phys. Status Solidi A, 1977, **44**, 621–626.
82 B. M. Wojek, P. Dziawa, B. J. Kowalski, A. Szczerbakow, A. M. Black-Schaffer, M. H. Berntsen, T. Balasubramanian, T. Story and O. Tjernberg, Phys. Rev. B, 2014, **90**, 161202(1)–161202(5).
83 E. El-Sayad, B. S. Farag and A. T. Amin, Vacuum, 2010, **84**, 807–811.
84 M. Saghir, A. M. Sanchez, S. A. Hindmarsh, S. J. York and G. Balakrishnan, Cryst. Growth Des., 2015, **15**, 5202–5206.
85 A. Rogalski and K. Jozwikowski, Phys. Status Solidi A, 1989, **111**, 559–565.
86 B. A. Efimova and L. A. Kolomoets, Sov. Ph. Solid State,

1965, **7**, 339–344.
87 B. A. Efimova, T. S. Stavitskaya, L. S. Stil'bans and L. M. Sysoeva, Sov. Ph. Solid State, 1960, **1**, 1217–1364.
88 I. V. Kucherenko, V. N. Moiseenko and A. P. Shotov, Sov. Phys. Semicond., 1977, **11**, 90–93.
89 I. V. Kucherenko and A. P. Shotov, Sov. Phys. Semicond., 1978, **12**, 1069–1071.
90 M. N. Vinogradova, S. V. Gurieva, S. V. Zarubo, L. V. Prokof'eva, V. I. Tamarchenko, T. T. Dedegkaev and T. B. Zhukova, Sov. Phys. Semicond., 1977, **11**, 902–904.
91 J. P. Heremans, V. Jovovic, E. S. Toberer, A. Saramat, K. Kurosaki, A. Charoenphakdee, S. Yamanaka and G. J. Snyder, Science, 2008, **321**, 554–557.
92 Y. Pei, A. LaLonde, S. Iwanaga and G. J. Snyder, Energy Environ. Sci., 2011, **4**, 2085–2089.
93 A. A. Coelho, Journal of Applied Crystallography, 2018, **51**, 210–218.
94 K. A. Borup, J. de Boor, H. Wang, F. Drymiotis, F. Gascoin, X. Shi, L. Chen, M. I. Fedorov, E. Muller, B. B. Iversen and G. J. Snyder, Energy Environ. Sci., 2015, **8**, 423–435.
95 S. Iwanaga, E. S. Toberer, A. LaLonde and G. J. Snyder, Rev. Sci. Instrum., 2011, **82**, 063905(1)–063905(6).
96 A. Volykhov, L. Yashina and V. I. Shtanov, Inorg. Mater., 2006, **42**, 596–604.
97 N. K. Abriksov, V. F. Bankina, L. V. Poretskaya, L. E. Shelimova and E. V. Skudnova, E. V. Skudnova, American Association for the Advancement of Science, 1969, p. 143.
98 H. Krebs, K. Grün and D. Kallen, Z. Anorg. Allg. Chem., 1961, **312**, 307–313.
99 R. Dornhaus, G. Nimtz and B. Schlicht, Narrow-gap semiconductors, Springer, 2006, vol. 98.
100 V. Shtanov, V. Zlomanov and A. Novoselova, Izv. Akad. Nauk SSSR Neorg. Mater., 1974, **10**, 224–227.
101 V. P. Zlomanov, W. B. White and R. Roy, Metall. Trans., 1971, **2**, 121–124.
102 J. C. Woolley and O. Berolo, Materials Research Bulletin, 1968, **3**, 445–450.
103 A. J. Strauss, Trans. Met. Soc. AIME, 1968, **242**, 354–365.
104 A. Totani, H. Okazaki and S. Nakajima, Tran. Metall. AIME, 1968, **242**, 709–712.
105 H. Liu and L. L. Chang, J. Alloys Compd., 1992, **185**, 183–190.
106 A. Laugier, Rev. Phys. Appl., 1973, **8**, 259–270.
107 J. Steininger, J. Appl. Phys., 1970, **41**, 2713–2724.
108 J. W. Wagner and J. C. Woolley, Mater. Res. Bull., 1967, **2**, 1055–1062.
109 N. K. Abrikosov, K. A. Dyul'dina and T. A. Danilin, Zh. Neorg. Khim., 1958, **1**, 1055–1062.
110 V. Kuznetsov, A. Gaskov and V. Zlomanov, Inorg. Mater., 1987, **23**, 804–808.
111 V. Leute and H.-J. Köller, Z. Phys. Chem., 1986, **149**, 213–227.
112 J. Steininger and A. J. Strauss, J. Cryst. Growth, 1972, **13-14**, 657–662.
113 J. Steininger, J. Appl. Phys., 1970, **41**, 2713–2724.
114 D. E. Grimes, Trans. Metall. Soc. AIME, 1965, **233**, 1442.
115 E. Elaguina and N. Abrikosov, Dokl. Akad. Nauk SSSR, 1956, **111**, 353–354.
116 M. Ocio, Phys. Rev. B, 1974, **10**, 4274–4283.
117 S. Ohno, K. Imasato, S. Anand, H. Tamaki, S. D. Kang, P. Gorai, H. K. Sato, E. S. Toberer, T. Kanno and G. J. Snyder, Joule, 2018, **2**, 141–154.
118 S. Ohno, U. Aydemir, M. Amsler, J.-H. Pöhls, S. Chanakian, A. Zevalkink, M. A. White, S. K. Bux, C. Wolverton and G. J. Snyder, Adv. Funct. Mater., 2017, **27**, 1606361(1)–1606361(1).
119 C. M. Crawford, B. R. Ortiz, P. Gorai, V. Stevanovic and T. S. Eric, J. Mat. Chem. A, 2018, **6**, 24175–24185.
120 B. R. Ortiz, K. Gordiz, L. C. Gomes, T. Braden, J. M. Adamczyk, J. Qu, E. Ertekin and E. S. Toberer, J. Mat. Chem. A, 2019, **7**, 621–631.
121 A. Goyal, P. Gorai, E. S. Toberer and V. Stevanović, NPJ Comput. Mater., 2017, **3**, 42(1)–42(9).
122 D. B. Chesnokova and M. I. Kamchatka, Inorg. Mater., 2001, **37**, 111–118.
123 S. Bajaj, G. S. Pomrehn, J. W. Doak, W. Gierlotka, H.-j. Wu, S.-W. Chen, C. Wolverton, W. A. Goddard and G. J. Snyder, Acta Mater., 2015, **92**, 72–80.
124 J.-C. Lin, T. L. Ngai and Y. A. Chang, Metall. Trans. A, 1986, **17**, 1241–1245.
125 R. Brebrick, J. Phys. Chem. Solids, 1963, **24**, 27–36.
126 R. Brebrick and A. Strauss, Phys. Rev., 1963, **131**, 104.
127 V. Vedeneev, S. Krivoruchko and E. Sabo, Semiconductors, 1998, **32**, 241–244.
128 N. Wang, D. West, J. Liu, J. Li, Q. Yan, B.-L. Gu, S. B. Zhang and W. Duan, Phys. Rev. B, 2014, **89**, 045142.
129 V. V. Prokopiv, L. V. Turovska, L. I. Nykyruy and I. V. Horichok, Chalcogenide Lett., 2016, **13**, 309–315.
130 E. Rogacheva, Nonstoichiometry and Properties of SnTe Semiconductor Phase of Variable Composition, IntechOpen, Rijeka, 2012.
131 K. Biswas, J. He, I. Blum, C.-I. Wu, T. P Hogan, D. Seidman, V. P Dravid and M. G Kanatzidis, Nature, 2012, **489**, 414–418.
132 J. O. Dimmock, I. Melngailis and A. J. Strauss, Phys. Rev. Lett., 1966, **16**, 1193–1196.
133 A. I. Dmitriev, G. V. Lashkarev, V. B. Orletskii and K. D. Tovstyuk, Phys. Status Solidi B, 1986, **135**, 587–596.
134 I. U. Arachchige and M. G. Kanatzidis, Nano Lett., 2009, **9**, 1583–1587.
135 Y. Tanaka, T. Sato, K. Nakayama, S. Souma, T. Takahashi, Z. Ren, M. Novak, K. Segawa and Y. Ando, Phys. Rev. B, 2013, **87**, 155105(1)–155105(5).
136 S.-Y. Xu, C. Liu, N. Alidoust, M. Neupane, D. Qian, I. Belopolski, J. Denlinger, Y. Wang, H. Lin, L. a. Wray et al., Nat. Commun., 2012, **3**, 1192(1)–1192(9).
137 K. Mitrofanov, A. Kolobov, P. Fons, M. Krbal, J. Tominaga

and T. Uruga, J. Phys. Cond. Matter, 2014, **26**, 475502(1)–475502(6).

138 Z.-Y. Ye, H.-X. Deng, H.-Z. Wu, S.-S. Li, S.-H. Wei and J.-W. Luo, NPJ Comput. Mater., 2015, **1**, 15001(1)–15001(6).

139 T. Hwa-wei Hsieh, H. Lin, J. Liu, W. Duan, A. Bansil and L. Fu, Nat. Commun., 2012, **3**, 982(1)–982(6).

140 A. D. LaLonde, Y. Pei, H. Wang and G. J. Snyder, Materials Today, 2011, **14**, 526 – 532.

141 Z.-Y. Li, M. Zou and J.-F. Li, J. Alloys Compd., 2013, **549**, 319–323.

142 R. J. Korkosz, T. C. Chasapis, S.-h. Lo, J. W. Doak, Y. J. Kim, C.-I. Wu, E. Hatzikraniotis, T. P. Hogan, D. N. Seidman, C. Wolverton, V. P. Dravid and M. G. Kanatzidis, J. Am. Chem. Soc., 2014, **136**, 3225–3237.

143 B. Abeles, Phys. Rev., 1963, **131**, 1906–1911.

144 B. R. Ortiz, H. Peng, A. Lopez, P. A. Parilla, S. Lany and E. S. Toberer, Phys. Chem. Chem. Phys., 2015, **17**, 19410–19423.

145 H. Xie, H. Wang, Y. Pei, C. Fu, X. Liu, G. J. Snyder, X. Zhao and T. Zhu, Adv. Funct. Mater., 2013, **23**, 5123–5130.

146 Y. Pei, H. Wang, Z. M. Gibbs, A. D. LaLonde and G. J. Snyder, NPG Asia Mater., 2012, **4**, e28(2)–e28(6).

147 Z. Liu, J. Mao, T.-H. Liu, G. Chen and Z. Ren, MRS Bulletin, 2018, **43**, 181–186.

148 H. Goldsmid and R. Douglas, Br. J. Appl. Phys., 1954, **5**, 386–390.

149 R. Chasmar and R. Stratton, J. Electron. Control, 1959, **7**, 52–72.

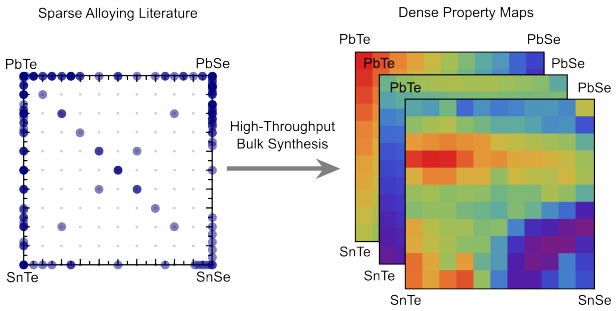

Despite extensive research, much of PbSnTeSe alloying space is unexplored. High-throughput bulk synthesis augments literature with high-resolution (121 sample) property maps.